Dhaka Univ. J. Sci. 74(2): 207–218, 2026 (July)
ISSN 1022-2502, E-ISSN 2408-8528
DOI: https://doi.org/10.3329/dujs.v74i2.83855

Evaluating Airfoil Performance: A Comparative Study Using Numerical Simulations of Two Airfoils

Muddachsir Rahman and M. Z. I. Bangalee*

Department of Applied Mathematics, University of Dhaka, Dhaka-1000, Bangladesh

(Received: 21 August 2025; Accepted: 1 February 2026)

Abstract

This study examines the aerodynamic performance of airfoils using numerical simulations. It compares pressure distributions, velocity profiles, and lift and drag coefficients of two airfoils, one is symmetric and another is cambered. The cambered airfoil produces higher lift due to increased pressure gradients near the leading edge but also incurs higher drag compared to the symmetric. The symmetric airfoil, with its uniform pressure distribution and lower drag, is suitable for applications prioritizing drag reduction. The findings highlight the cambered's advantage in high-lift scenarios, while the symmetric offers a balanced performance with lower drag. These insights aid in selecting airfoils for various aerodynamic applications. Future research could explore different flow conditions, turbulence models, and three-dimensional effects for deeper analysis.

Keywords: CFD; airfoil; lift co-efficient; drag co-efficient; NACA 0012; NACA 4412

I. Introduction

Human flight has long been a pursuit of science, driven by curiosity, ambition, and the desire to transcend natural limitations. Unlike birds, humans lack biological structures capable of generating lift or thrust; thus, technological innovation became essential for realizing controlled flight. This aspiration culminated in the early 20th century, when pioneers such as the Wright brothers—who conducted systematic wind tunnel tests to determine wing camber and curvature—and Alberto Santos-Dumont—whose *14-bis* demonstrated sustained powered flight—laid the foundation of modern aeronautics[1]. Since then, continuous advancements in fluid dynamics, propulsion, and structural design have shaped aviation into a critical domain of engineering and science.

A central element of flight is the airfoil, the cross-sectional shape of a wing or blade, which dictates aerodynamic performance by influencing lift, drag, and stability. Early studies, such as Schmitz's experiments in the 1930s on thin plates and cambered profiles, highlighted the importance of Reynolds number effects on aerodynamic behaviour at both high and low flow regimes[2]. Subsequent research has expanded these investigations using computational fluid dynamics (CFD) and advanced turbulence modelling. For example, Liyana et al.[3] employed a k–ω SST turbulence model for NACA 2412 analysis, while Lehmkuhl et al.[4] validated sub-grid-scale models against DNS data to study transition and turbulence. These approaches have revealed complex phenomena such as laminar separation bubbles (LSBs), vortex shedding, and boundary-layer reattachment[5]. Such insights are particularly relevant to modern applications including micro aerial vehicles (MAVs), unmanned aerial vehicles (UAVs), and planetary exploration missions, where aerodynamic efficiency at low Reynolds numbers is critical[6].

Among the numerous airfoil families, the NACA airfoils have been extensively studied and widely adopted in aeronautical and engineering applications[7]. Two profiles of particular interest are the NACA 0012, a symmetric airfoil often used as a baseline reference due to its geometric simplicity[8], and the NACA 4412, a cambered airfoil known for its enhanced lift performance[9]. The camber of the NACA 4412 provides favorable aerodynamic characteristics across a wide range of operating conditions, making it suitable for both conventional aircraft and renewable energy systems such as wind turbines[10]. Prior research has investigated turbulence models, stall behaviour, and flow separation mechanisms for these airfoils[11–13]. However, despite this body of work, there remains a lack of direct comparative studies analyzing the aerodynamic performance of symmetric versus cambered airfoils under comparable flow conditions, particularly at high Reynolds numbers relevant to practical aviation.

This study addresses that gap by conducting a comparative CFD analysis of the NACA 0012 and NACA 4412 airfoils across a range of angles of attack at a Reynolds number of six million, corresponding to turbulent flow conditions. Using the Spalart–Allmaras turbulence model within ANSYS Fluent, the analysis evaluates lift, drag, pressure distribution, and velocity contours, while also assessing the impact of mesh quality on simulation accuracy. By systematically contrasting symmetric and cambered geometries, this work provides insights into the aerodynamic trade-offs between stability and lift efficiency. The findings contribute to the optimization of airfoil selection in aerospace design and renewable energy

* Author for correspondence. e-mail: zavid@du.ac.bd

applications, where achieving a balance between aerodynamic efficiency and structural reliability is critical.

II. Equations, Geometry and Modeling

Spalart-Allmaras (SA) Turbulence Model

A modified turbulent viscosity is solved by a single transport equation in the SA model[14], a one-equation turbulence model. It works especially well in aerospace applications where boundary layer fluxes are present. The SA model is known for its efficiency and accuracy in predicting turbulent flow behaviour around airfoils, making it a preferred choice for this study. The model developed by Spalart and Allmaras (1992) is a simple one-equation method for solving a kinematic eddy transport equation (turbulent) viscosity. For boundary layers subjected to unfavourable pressure gradients, it has a history of delivering good results and was developed for aerospace wall-bounded flow applications. Aerodynamic flows were considered in the development of the Spalart-Allmaras Turbulence Model. This formulation combines a logarithmic formulation founded on y+ with a viscous sublayer formulation.

Consequently, the laminar/viscous sublayer simulation does not employ any significantly non-linear damping functions. Additionally, its use in turbomachinery applications is growing.Originally, it was essentially a low Reynolds number model that needed a good resolution of the viscous-affected portion of the boundary layer. The 1-equation eddy viscosity transport model was not derived in the same way as 2-equation models, which are often derived by means of rigorous mathematical operations that are subsequently simplified by physical reasoning. This is true for all other transport equations, including the Reynolds stresses. The mean strain rate determines the eddy viscosity.

$$\nu_t = \frac{\overline{u'v'}}{du/dy}$$

Eddy viscosity transfer is described by an equation that uses the words convection, diffusion, generation, and destruction.All of the various variables in the Spalart-Allmaras approach, including diffusion, production, and destruction, were assumed to be based on surgical physics in order to produce a comprehensive transport equation for the eddy viscosity[15].

$$\frac{D\nu_t}{Dt} = \text{Diffusion} + \text{Production} - \text{Destruction}$$

Compared to the models that employ them, the conveyed variable's near-wall gradients are less in this model.

The following defines the Spalart-Allmaras turbulence model's final form:

$$\frac{D\tilde{\nu}}{Dt} = c_{b1}\tilde{S}\tilde{\nu} + \frac{1}{\sigma}\left[\nabla.\left(\left(\nu+\tilde{\nu}\right)\nabla\tilde{\nu}\right) + c_{b2}\left(\nabla\tilde{\nu}\right)^2\right] - c_{w1}f_w\left[\frac{\tilde{\nu}}{d}\right]^2$$

In this case, the three terms on the equation's right side stand for production, destruction, and diffusion, respectively. The following are the Spalart-Allmaras model's empirical constants:

$$c_{w1} = 3.239; \quad c_{w2} = 0.3; \quad c_{w3} = 2;$$
$$\sigma = \frac{2}{3}; \quad c_{b2} = 0.622; \quad \left(1+c_{b2}\right)/\sigma \approx 2.4$$

The phase from g to the control function represents the limiter effect for the control function.

$$r \equiv \frac{\nu_t}{Sk^2d^2}; \quad l \equiv \sqrt{\nu_t / S}; \quad S = \frac{u_r}{kd};$$
$$\nu_t = u_r kd; \quad c_{w1} = c_{b1}/k^2 + \left(1+c_{b2}\right)/\sigma;$$
$$f_w(r) = g\left[\frac{1+c_{w3}^6}{g^6+c_{w3}^6}\right]^{1/6}; \quad g = r + c_{w2}(r^6 - r)$$

NACA 0012 is a symmetric airfoil; the 00 suggests that it does not have any camber.The number 12 indicates that its thickness to chord length ratio is 12%. Re = $6x10^6$ was chosen as the Reynolds number in this study for validating the present simulations. Simply its thickness is 12% of its length. The airfoil has a chord length of 1 m (1000 mm). By drawing a horizontal line along the airfoil's chord line and two vertical lines, one at (0.105, 0, 0) and the other at the trailing edge at (1, 0, 0), the domain has been separated into six surfaces for better control and a smoother transition throughout the mesh generation. The six surfaces were projected into the fluid domain using the projection tool.

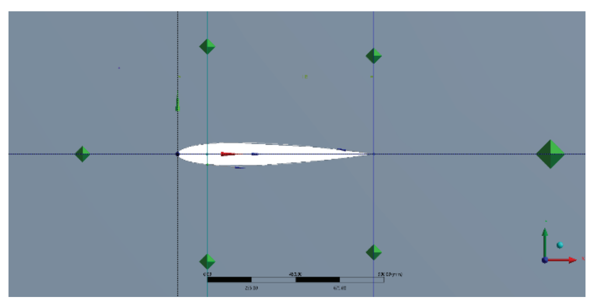

Fig. 1. Construction of the fluid domain for NACA 0012

The first number, "4" for NACA 4412, represents the airfoil's maximum camber expressed as a percentage of chord length. The maximum camber for the NACA 4412 airfoil is 4% of the chord length. The location of the greatest camber in tenths of the chord length is indicated by the second number, "4". 40% of the chord length from the leading edge is where the highest camber is found in this instance. The thickness-to-chord ratio for the NACA 4412 airfoil is 12%, as shown by the final two digits, "12". This means that at any point along the chord length, the distance from the top surface to the bottom surface of the airfoil is 12% of the chord length. These parameters define the shape of the airfoil, Aerodynamics and aircraft design depend on it. The NACA airfoil series, including the NACA 4412, has been extensively used in the design of aircraft wings and other Aerodynamic surfaces due to their well-defined characteristics and performance properties.

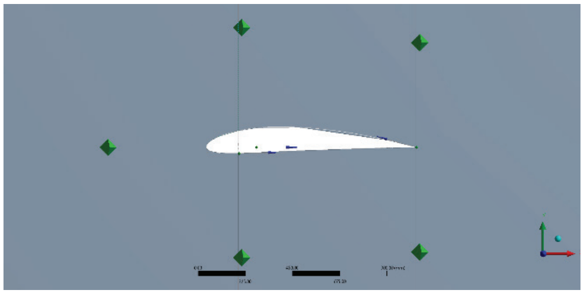

Fig. 2. Construction of the fluid domain for NACA 4412

Boundaries of the domain

By depleting the peripheral conditions of the flow field, the fluid domain has been initiated[16]. The finite element method discretizes the fluid domain[17] into smaller elements based on a specific geometry. Because it can offer greater precision than an unstructured mesh, a quadrilateral structured mesh has been utilized in the fluid domain[18]. The free stream velocity is set to 102 m/s. 288.16 K is taken as the freestream temperature for the study. The density of air at this temperature is 1.225 Kg/m^3, and the viscosity is 2.0825x10^{-5} Kg/m-s. The flow can be considered incompressible for this Reynolds number. This assumption is close to reality and thus the energy equation can be resolved. An implicit, segregated solver was used (ANSYS Fluent 2020 R1) for the simulations. For angles of attack of 0, 10, 15, and 20 degrees, calculations were performed. In areas where higher computational accuracy was required, such the airfoil's boundary layer, the mesh's resolution was finer. Checking the impact of mesh size on solver output is the first stage in running a CFD simulation. Normally, more nodes imply a more accurate outcome. But it also increases the computational time and memory.

Mesh Distribution

In this study, quadrilateral cells in a C-type grid structure[19] will be employed. The C-type pattern is an enhanced version of the H-type topology that captures the leading-edge curvature without any singularities. The C-type pattern does not prevent boundary layer fineness from propagating downstream of the airfoil trailing edge, although it does so upstream. The domain's height was fixed at ten chord lengths. The wall spacing for this velocity is 0.000008469 or 8.47x10^{-6} m and the desired y$^+$[20] is 1. The non-dimensional distance between the wall and the first mesh node is represented by the y+ value, which is dependent on the local cell fluid velocity, as shown in Fig. 3 below.

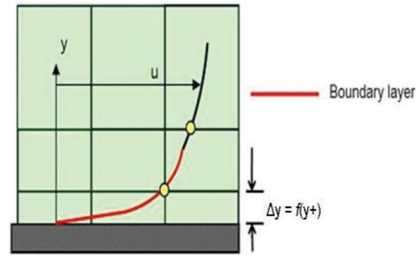

Fig. 3. Definition of y+.

A y$^+$ of this size is expected to resolve the inner parts of the boundary layer adequately. There is a total of 12 edges excluding the airfoil and different edge sizing have been implemented in each edge for a finer mesh quality. For improved accuracy and better flow visualization, to achieve a high mesh density around the airfoil, the bias factor has been used[21-22]. By meshing the whole domain of the geometry, there have 200900 of nodes and 200000 of elements. For making all structured quadrilateral grid and comparatively huge number of nodes and elements, it is expected a good approximation for numerical simulation. The test of grid independence at zero degree angle of attack is attached here.

Table 1. Grid Independence

Number of Elements	Number of Nodes	Drag Coefficient
70000	70500	0.00811
200000	200900	0.00812
375000	376300	0.00812

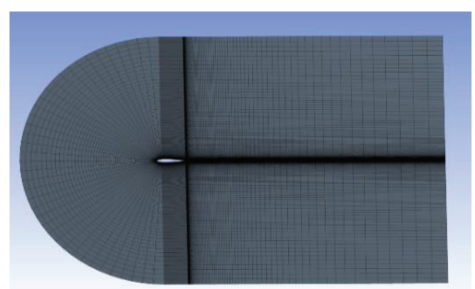

Fig. 4. Mesh generation of the fluid domain for NACA 0012.

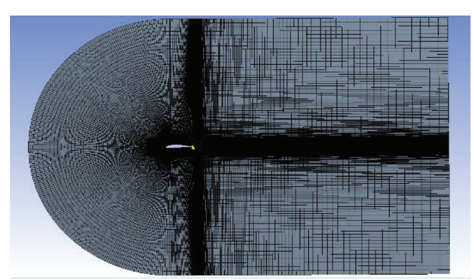

Fig. 5. Mesh generation of the fluid domain for NACA 4412.

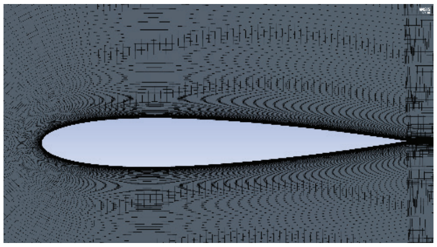

Fig. 6. Zoomed mesh of the fluid domain for NACA 0012

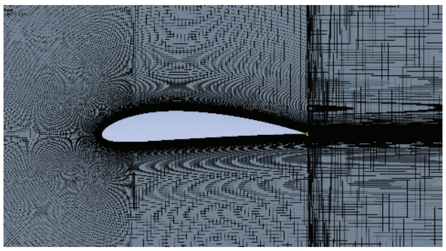

Fig. 7. Zoomed mesh of the fluid domain for NACA 4412

Structured meshing has been implemented in this study. Generally, a structured mesh consists of hex (brick) elements[23] (quads in 2D) that follows a uniform pattern.

A new method was employed in order to account for transition effects in the computation of the aerodynamic coefficients and provide precise findings for the drag coefficient. The transition point of the airfoil from laminar to turbulent flow was determined by dividing the computational mesh into two regions: laminar and turbulent. The transition point was identified using the following methodology. A perpendicular line was drawn at the transition point (x_{tr}), which was assigned a random value, to divide the computing domain. The problem was simulated in Fluent after the left and right regions were determined to be laminar and turbulent, respectively.

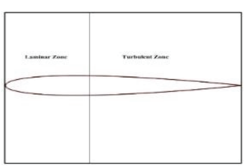

Fig. 8. Flow regions around the airfoil

A new transition point value that was higher than the original one had to be selected if the C_d simulation result was more than the actual data, indicating that the simulated turbulent zone was larger than the real one. If the c simulation result was less than the experimental data, the transition point was further to the left and the simulated turbulence zone was smaller than the real one.This method was used repeatedly until two -simulated outcomes that met the inequality were obtained $C_{d,sim1}<C_{d,exp}<C_{d,sim2}$ and $x_{tr1}<x_{tr}<x_{tr2}$, the simulated and experimental data were more similar. The appropriate x_{tr} resulted from the linear interpolation of the mentioned values.

Solver Setup and Boundary Conditions

Solver Setup**:** The system has to have boundary conditions defined before the calculations can begin. The ANSYS Fluent setup program is used for setup. Selecting the ideal study model is the initial stage of setup. For the 2-D simulations, the Spalart-Allmaras viscous model has been selected.In this simulation, two materials are being used. Air is a fluid in the first instance, and aluminium is a solid in this instance. Aluminium has a density of 2719 kg/m^3.

Boundary conditions: At inlet, the velocity specification method has been established using magnitude and direction. The magnitude of the freestream velocity is 10^2 m/s, and the reference frame is absolute. 0 N/m^2 is the initial gauge pressure. The intensity and viscosity ratio is the turbulence specification approach that is used. There is a 5% turbulent intensity and a 10% turbulent viscosity ratio.At outlet, he reference frame for absolute backflow has been chosen. The gauge pressure at the outflow is $0N/m^2$.The multiplier for pressure profiles is set to 1. Backflow turbulent intensity is adjusted to 5% and backflow turbulent viscosity ratio to 10, using intensity and viscosity ratio as the turbulence specification technique.

Reference Values: Inlet data is used to calculate reference values. These are the values:

Table 2. Reference Values

Area (m^2)	1
Depth (m)	1
Enthalpy (j/kg)	0
Density (kg/m^3)	1.225
Length (m)	1
Pressure (N/m^2)	0
Viscosity (kg/m-s)	$2.0825\text{x}10^{-5}$
Temperature (k)	288.16
Velocity (m/s)	102
Ratio of Specific Heats	1.4

Initialization

The solution can be initialized in one of two ways: configure the entire flow field (in every cell) and apply functions or patch values to specific flow variables in certain cell zones or cell "registers."(Registers are constructed using the same functions that label cells for adaptation). All of the variables are specified as initial guesses using standard initialization. Fluent is configured to allow the user to establish the initial temperature, pressure, x-, y-, and z-velocities, as well as other parameters, as constant fields over the entire domain. While hybrid initialization solves a simplified equation system for the number of repetitions (10), standard initialization only fills the field characteristics with constant values. This results in a superior prediction for the flow variables, especially the pressure field. Hybrid initialization should be used whenever possible because it usually speeds up the total computation.Therefore, in this study, hybrid initialization has been used. After initializing, 10 iterations are produced which are later imported to the calculation process for running the calculation.

III. Numerical Solutions

In this study, the Spalart-Allmaras equation has been solved using a higher resolution technique. The solution approach employs a linked scheme. The pressure is set to order of two, and the gradient is set to least square cell based. Momentum is treated using a second order upwind discretization. A similar discretization for changed turbulent viscosity is used. For this approach, pseudo transience has been turned off. During the calibration process, experimental and numerical findings from the type of flow that needs to be modeled are used to determine constants and functions. The numerical approach is implemented with a computer solver called FLUENT[24]. The discretions of cell center and finite volume serve as the foundation for the solution. Blocks of calculations are performed, and each block is divided into tetrahedral cells. The second-order precision Time is discredited by using Gear's concept[25] of the fully implicit scheme.

Convergence Conditions

There are four requirements for convergence: force, displacement, moment, and rotation. By using one of them, a value, a tolerance, and a minimum reference can be given. This final parameter, which indicates that the situation has never converged, is set to void when the value is approaching zero. In general, the force which includes force, displacement, rotation, and moment is regarded as convergence criteria. A value, a tolerance, and a minimum reference may be provided when using one of these. This final parameter is meant to prevent a never-converged scenario when the value is near zero. The ANSYS Fluent residual monitors have been used to set the convergence criteria for the current investigation. The set of 10^{-7} is the absolute criterion for continuity in this case. Since all the other parameters will converge if the numerical solution turns out to be continuous, just the convergence of continuity will be examined. In essence, convergence criteria are a way for the solution to eliminate nonlinear properties to ensure the end run.

The residual graphs alter for varying angles of attack. The graphs displayed here illustrate the continuity, x-, y-, and nut velocities for Re = 6000000. Below are the residual graphs for 0 and 10 degree angles of attack. Each of the simulations that follow has 1000 iterations averaged across ten step intervals.

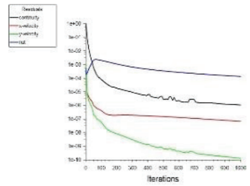

Fig. 9. Residuals at $\alpha = 0°$ for NACA 0012

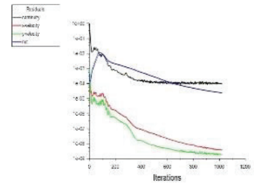

Fig. 10. Residuals at $\alpha = 10°$ for NACA 0012

As shown in the figures above, continuity in each graph has an overall downward slope. This implies that continuity holds for each simulation and the system will have a convergent output.

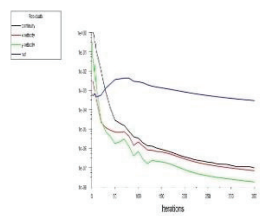

Fig. 11. Residuals at $\alpha = 0°$ for NACA 4412

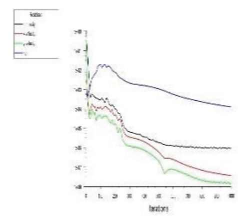

Fig. 12. Residuals at $\alpha = 10°$ for NACA 4412

Convergence of Lift and Drag Coefficients

Lift and drag forces are two of the governing forces in any study of Aerodynamics. At various angles of attack, the lift and drag over the same airfoil will change. At a certain angle of attack, the lift and drag coefficients converge to a particular value.The following graphs illustrate how C_d and C_l converge at 0 and 10 degrees of angle of attack.

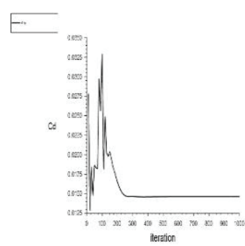

Fig. 13. Convergence of C_d at α =10°for NACA 0012

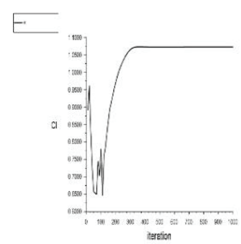

Fig. 14. Convergence of $C_l$at $\alpha = 10°$ for NACA 0012

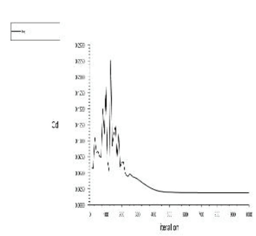

Fig. 15. Convergence of C_d at $\alpha = 10°$ for NACA 4412

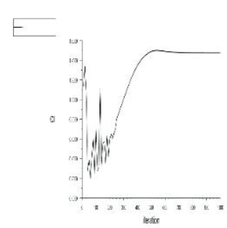

Fig. 16. Convergence of C_l at $\alpha = 10°$ for NACA 4412

Stall Phenomena

A stall occurs when an airfoil's angle of attack exceeds the value that results in the most lift from airflow across it. This angle is normally around 15° and varies very little in response to the cross section of the (clean) airfoil. At the stall, the airflow across the upper cambered surface stops flowing smoothly and in contact with the upper surface and becomes turbulent, lowering lift and increasing drag significantly. Using leading edge or trailing edge devices to change the effective configuration of a wing will change the angle of attack at which an airfoil stall. All of this, however, presupposes a clean wing, and contamination of the ordinarily smooth surface by frozen deposits will cause a shift in the angle of attack at which a stall will occur for any airfoil.

At 20 degrees angle of attack, the graphs of convergence of C_d and C_l are shown below:

The values of C_d and C_l both converge to a certain value in the figures above up to a specific angle of attack. That angle of attack is 15 degrees. As AoA is increased from 15 degrees, the convergence criterion for lift and drag starts to crumble. The reason behind this phenomenon is stall.

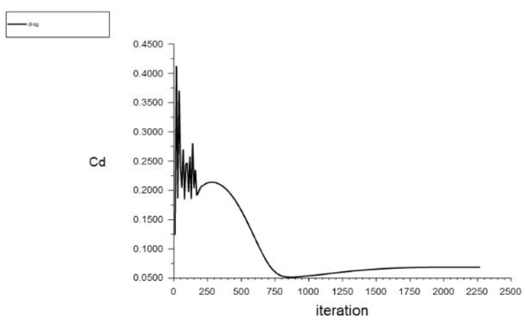

Fig. 17. Pseudo convergence of C_d at α=20° for NACA 0012

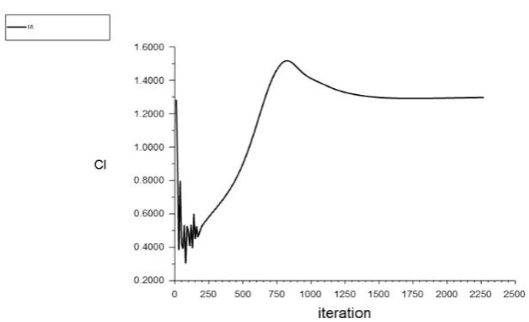

Fig. 18. Pseudo convergence of C_l at α = 20° for NACA 4412

As shown in the Fig. 17 and 18, neither C_d nor C_l converges to a specific value because the angle of attack the airfoil is operating at is 20 degrees which is way above the stall angle of attack.

Validation

Corresponding to changes in angles of attack, the values of C_d and C_l also change. At Re = $6x10^6$, the relationship between angles of attack and coefficients of lift and drag are shown in the tables and graphs below.

Table 3. Lift coefficient, C_l at various angle of attack(AoA)

Angles of Attack (In Degree)	Lift Coefficient, C_l
0	0
3.85	0.4212
5	0.5459
5.90	0.6439
7.96	0.8623
10	1.0725
10.18	1.0916
11.05	1.1773
13.11	1.3746
15	1.5393
16.38	1.6439
16.57	1.4044
17.29	1.0903
20	1.2970

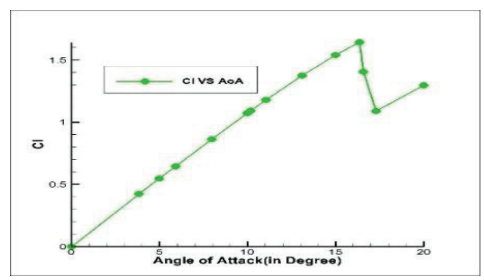

Fig. 19. Coefficient of lift vs angle of attack for NACA 0012

Table 4. Lift coefficient, C_l validation at various angle of attack(AoA)

AoA	Present	Abbott[26]	Error (%)
0	0	0	0
5.90	0.6439	0.6466	0.4214
10.12	1.0916	1.1207	2.5968
13.11	1.3746	1.3625	0.8881
16.38	1.6439	1.5959	3.0079
16.57	1.4044	1.4244	1.4049

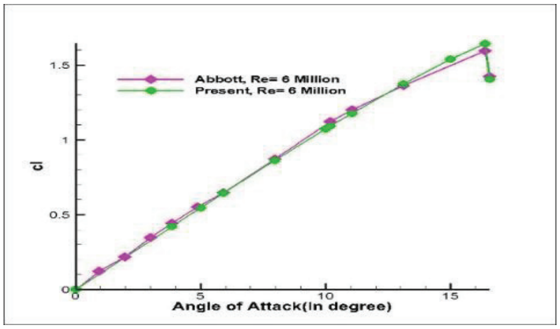

Fig. 20. Coefficient of lift vs angle of attack (Validation)

Table 5. Drag coefficient, c_d validation at various angle of attack(AoA)

AoA	Present	Li[27]	Error(%)
0	0.0081	0.0079	1.9785
3.85	0.0091		
5	0.0097	0.0100	3.3725
6	0.0104		
7.96	0.0122		
9	0.0134		
10	0.0147	0.0150	2.1314
11.05	0.0162		

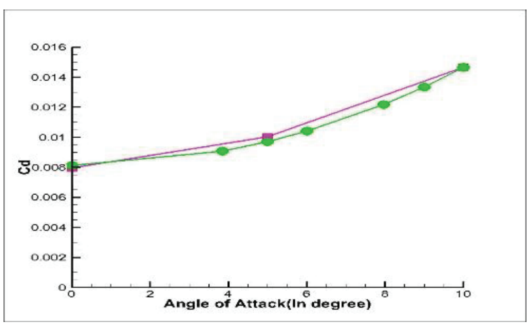

Fig. 21. *Coefficient of drag vs angle of attack (Validation)*

IV. Results and Discussions

Acceptable results require a well-converged solution. A convergent solution can only be found with a small mesh topology. Therefore, CFD is employed to produce high-quality meshes in this investigation.

Results

With a 5° increment, the solutions for angles of attack between 0° and 15° have been found. Investigating the change in lift coefficient (C_l) and drag coefficient (C_d) at various angles of attack (AoA) at Re = $6x10^6$ is the aim of the current study. This study has also shown the corresponding behaviour of pressure, velocity, and turbulence. One thing needs to be kept in mind in order to produce a turbulent airflow. That instance, for a turbulent flow, the Reynolds number is extremely high.

Contours

Plotting profiles or contour lines throughout the physical domain is feasible. The lines of constant magnitude for a given variable are called contour lines. A profile plot is used to construct these contours, which are projected off the surface proportionate to the value of the plotted variable at each location on the surface. Pressure contours for Re = 6 million over the NACA 0012 airfoil are shown below, with a 5° increase, for angles of attack between 0° and 20°.

Pressure Contours for NACA 0012

The following displays pressure contours over the NACA 0012 airfoil at angles of attack with a 5° increase for Re = 6 million, from 0° to 20°.

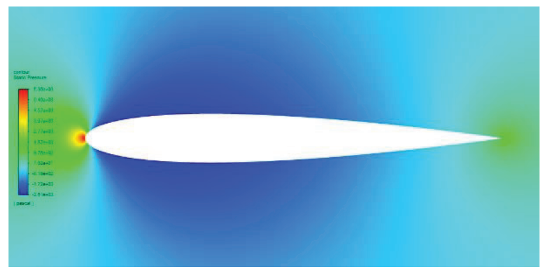

Fig. 22. Contour of pressure at α=0°

Fig. 23. Contour of pressure at α=5°

Fig. 24. Contour of pressure at α=10°

Fig. 25. Contour of pressure at α=15°

Fig. 26. Contour of pressure at α=20°

The aforementioned figures show the static pressure's contours. At a 0° angle of attack, it is evident that the pressure distribution surrounding the airfoil is the same on the top and lower surfaces. When the angles of attack are raised by 5°, the pressure acts differently. For α=5°, the pressure near the bottom of the leading edge is greater than the pressure at the same point for α=0°. The pressure at α=10° is greater than that at α=5° at the same location. Similarly, at α=10°, α=15°, and α=20°, pressure gradually rises at the same location near the leading edge.In proportion to the pressure at the bottom surface, the pressure at the top surface drops. Because the pressure on the top and bottom surfaces increases and decreases simultaneously, lift and drag increase until the stall angle.

Velocity Contours for NACA 0012

For Re = 6 million, the following velocity contours are over the NACA 0012 airfoil with 5° increments between 0° and 20° angles of attack.

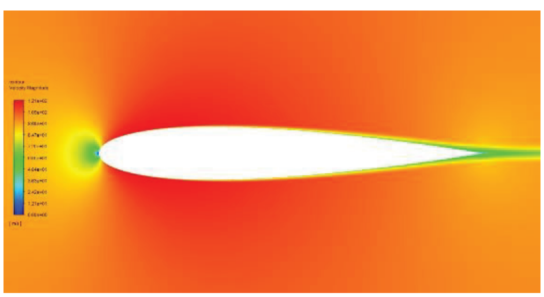

Fig. 27. Contour of velocity at α=0°

Fig. 28. Contour of velocity at α=5°

Fig. 29. Contour of velocity at α=10°

Fig. 30. Contour of velocity at α=15°

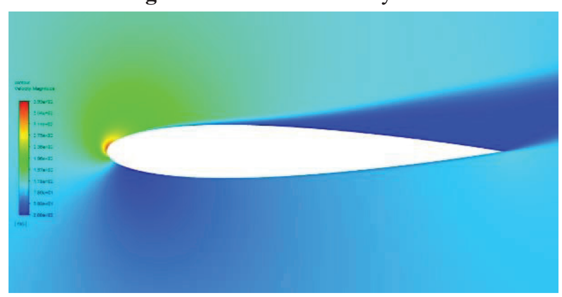

Fig. 31. Contour of velocity at α=20°

It is evident from the velocity contours above that, with varying angles of attack, velocity also varies around the airfoil. The airfoil's leading edge has a stagnation point at α=0°. At a 0° angle of attack, the flow separation surrounding the airfoil is symmetrical. A 5° rise in α causes the stagnation point to shift. Lift is produced and C_l rises simultaneously. The lift coefficient keeps increasing as the value of α rises. The connection between pressure and velocity is inverse. Velocity will fall with increasing pressure and vice versa. The coefficient of lift will begin to drop as soon as the stall angle is crossed, but the coefficient of velocity will grow gradually up to the stall angle.

Turbulence Contours for NACA 0012

The following shows the turbulence contours over the NACA 0012 airfoil at 0° to 20° angles of attack for Re=6 million with a 5° increase.

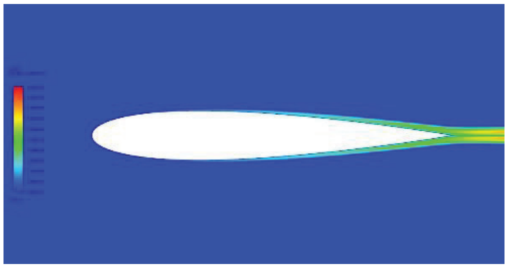

Fig. 32. Contour of turbulence at α=0°

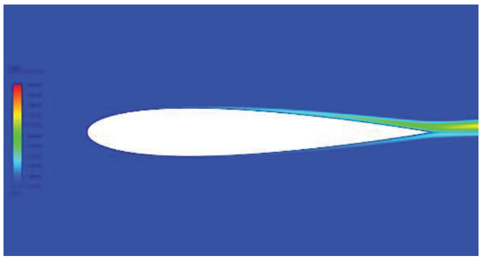

Fig. 33. Contour of turbulence at α=5°

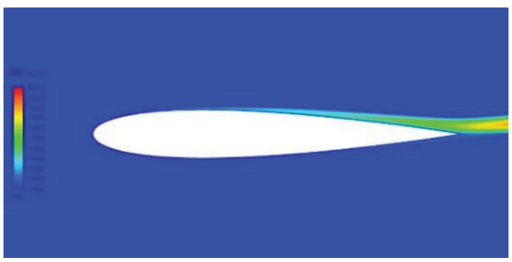

Fig. 34. Contour of turbulence at α=10°

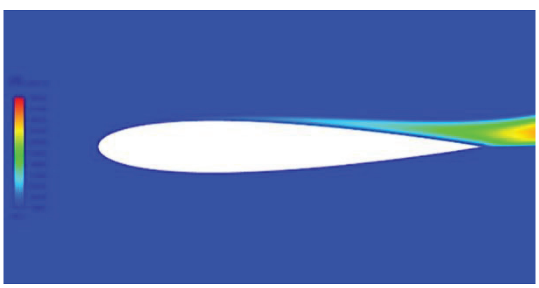

Fig. 35. Contour of turbulence at α=15°

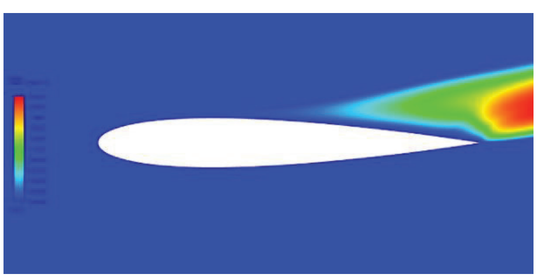

Fig. 36. Contour of turbulence at α=20°

It is observed that turbulence varies with angle of attack. At the trailing edge, the impact of turbulence is more noticeable than at the leading edge. The turbulence is symmetric around the airfoil when α=0°. The turbulence begins to shift dramatically as the angle of attack increases.The following displays pressure contours over the NACA 4412 airfoil at angles of attack with a 5° increase for Re = 6 million, from 0° to 15°.

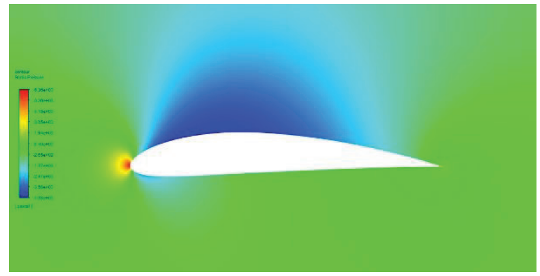

Fig. 37. Contour of pressure at α=0°

Fig. 38. Contour of pressure at α=5°

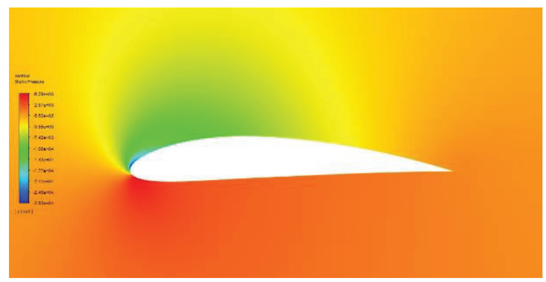

Fig. 39. Contour of pressure at α=10°

Fig. 40. Contour of pressure at α=15°

The contours of the static pressure are depicted in the diagrams above. It is clear that the pressure distribution around the airfoil is the same on the upper and lower surfaces at a 0° angle of attack. The pressure behaves differently when the angles of attack are increased by 5°. When the angle is 5°, the pressure at the bottom of the leading edge is higher than when the angle is 0°. At the same place, the pressure is higher at α=10° than it is at α=5°. Likewise, pressure progressively increases at the same spot close to the leading edge for α=10° and α=15°.

The pressure at the top surface decreases in proportion to the pressure at the bottom surface. Lift and drag grow until the stall angle because the pressure on the top and bottom surfaces rises and falls at the same time.For Re=6 million, the following velocity contours are over the NACA 4412 airfoil at angles of attack with a 5° increase for Re=6 million, from 0° to 15°.

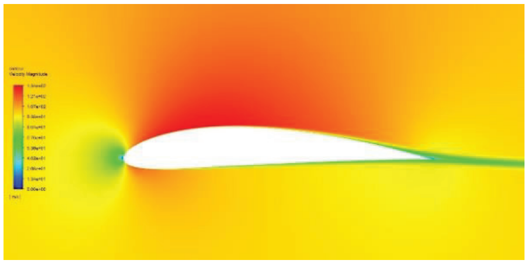

Fig. 41. Contour of velocity at α=0°

Fig. 42. Contour of velocity at α=5°

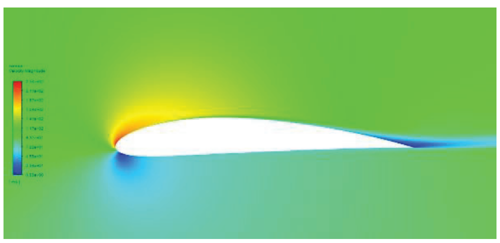

Fig. 43. Contour of velocity at α=10°

Fig. 44. Contour of velocity at α=15°

The velocity contours above make it clear that velocity fluctuates around the airfoil with different angles of attack. The stagnation point of the leading edge of the airfoil is located at α=0°. The flow separation around the airfoil is symmetrical at a 0° angle of attack. The stagnation point changes with a 5° increase in α. C_l increases along with the production of lift. As the value of α increases, the lift coefficient continues to grow.

Pressure and velocity have an inverse relationship. As pressure increases, velocity will decrease, and vice versa. When the stall angle is crossed, the coefficient of lift will start to decrease, but the coefficient of velocity will increase progressively until it reaches the stall angle. The connection between pressure and velocity is inverse. Velocity will fall with increasing pressure and vice versa. The coefficient of lift will begin to drop as the stall angle is crossed, while the coefficient of velocity will gradually rise until it hits the stall angle.

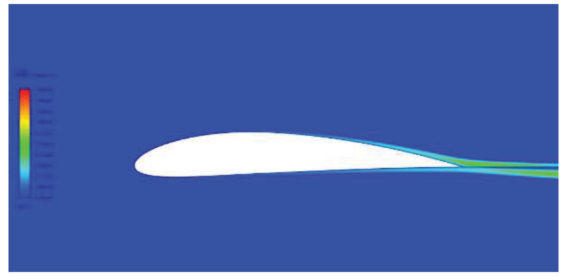

Fig. 45. Contour of turbulence at α=0°

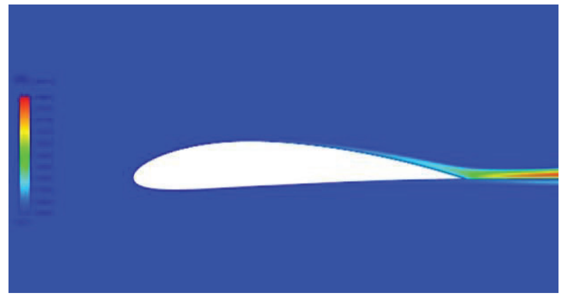

Fig. 46. Contour of turbulence at α=5°

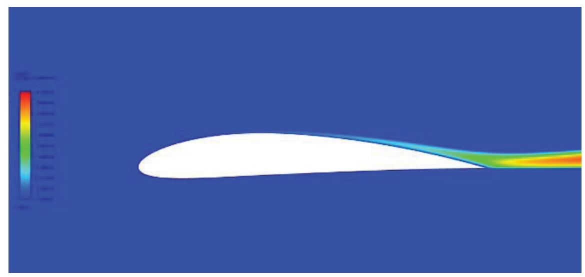

Fig. 47. Contour of turbulence at α=10°

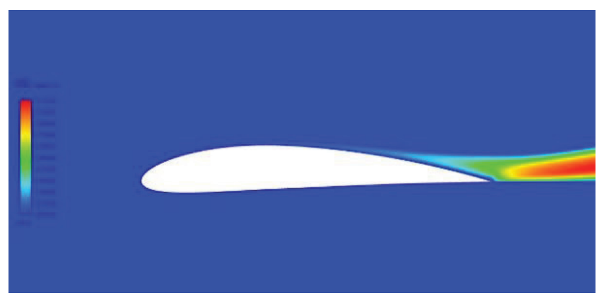

Fig. 48. Contour of turbulence at α=15°

It has been noted that the angle of attack affects turbulence. Turbulence has a more pronounced effect at the following edge than at the leading edge. When α=0°, the turbulence is symmetric around the airfoil. When the angle of attack rises, the turbulence starts to change significantly.

Comparison of Lift and Drag

Comparison in Case of Zero Degree Angle

Both the NACA 0012 and NACA 4412 airfoils are functioning in a comparatively low-lift, low-drag zone at an angle of attack of 0 degrees. The coefficients of lift (C_l) and drag (C_d) for these airfoils at this angle are qualitatively compared here: Because it is symmetrical, the NACA 0012 airfoil produces lift mainly through angle of attack. It generates a mild lift force at an angle of attack of 0 degrees. In comparison to higher angles of attack, the NACA 0012's drag coefficient (C_d) at 0 degrees is comparatively low. However, because of its rather thick profile, it may still show a little bit more drag than other symmetrical airfoils at the same angle. Given the moderate lift produced by the airfoil at this angle, the NACA 0012's lift coefficient (C_l) at 0 degrees angle of attack would also be mild.

Due to its cambered shape, the NACA 4412 airfoil produces some lift even at an angle of attack of zero degrees. At low angles of attack, this camber enables more effective lift production than symmetrical airfoils. Because of the camber, which can result in a slightly greater pressure differential between the airfoil's upper and lower surfaces, the NACA 4412's drag coefficient at a 0 degree angle of attack may be somewhat higher than the NACA 0012's. For its cambered design, which allows for more effective lift production even at low angles of attack, the NACA 4412's lift coefficient at 0 degrees angle of attack would probably be marginally higher than the NACA 0012's.

Comparison in Case of Stall Angles

Both airfoils show moderate lift and comparatively little drag at 0 degrees angle of attack. Because of its cambered shape, the NACA 4412 airfoil may have a minor lift coefficient advantage over the NACA 0012, but it may also have a slightly greater drag. However, at such low angles of attack, these variations would probably be minor and might not have a big effect on overall performance. Experimental data or computer simulations would be needed to provide precise numerical figures for the coefficients of drag (C_d) and lift (C_l) for the NACA 0012 and NACA 4412 airfoils at specified stall angles. On the basis of these airfoils' attributes, I may provide a broad qualitative comparison, though:

The symmetrical NACA 0012 airfoil would probably see a sudden and dramatic drop in lift and an increase in drag as flow separation takes place over both upper and lower surfaces at a stall angle of 16.37 degrees. Because of its symmetrical shape, the NACA 0012's lift coefficient at stall would be comparatively lower than that of cambered airfoils like the NACA 4412. The tendency of the symmetrical airfoil to show more drag at stall circumstances may result in a comparatively higher drag coefficient at stall for the NACA 0012. With its cambered shape, the NACA 4412 airfoil would probably stall more gradually than the NACA 0012 at a stall angle of 13.87 degrees. When compared to a symmetrical airfoil, the camber can increase lift coefficients (C_l max) by delaying the separation of airflow over the upper surface.

The camber of the NACA 4412 airfoil provides for improved lift generation and perhaps delayed stall behaviour, which may result in a slightly higher lift coefficient at stall than the NACA 0012. By delaying stall and perhaps reducing drag development, the cambered shape of the NACA 4412 may have a somewhat lower drag coefficient at stall than the NACA 0012.Overall, the cambered shape of the NACA 4412 usually permits better lift coefficients and possibly lower drag coefficients at stall compared to the symmetrical NACA 0012 airfoil, even though both the NACA 0012 and NACA 4412 airfoils experience stall conditions at different angles of attack. However, precise numerical values would require computational analysis or experimental testing and would depend on a number of variables.

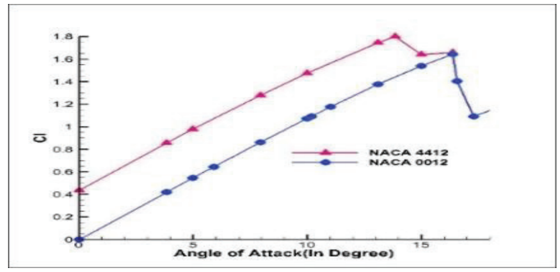

Fig. 49. C_l of NACA 0012 and NACA 4412

V. Conclusion

The NACA 0012 and NACA 4412 airfoils' aerodynamic performance under subsonic conditions has been better understood thanks to the numerical simulation work conducted at Mach number 0.3. To comprehend the performance variations between the two airfoil designs, the main aerodynamic parameters—lift, drag, and pressure distributions—are examined using exacting computational fluid dynamics (CFD) simulations. The findings show that although the lift and drag coefficient trends of the two airfoils are similar, their aerodynamic properties differ noticeably. In comparison to the NACA 0012 airfoil, the NACA 4412 airfoil exhibits a marginally higher maximum lift coefficient, suggesting greater lift capabilities and possibly better performance under specific operating conditions. Nonetheless, the NACA 0012 airfoil shows reduced drag coefficients at different angles of attack, indicating better drag generating efficiency.

Additionally, differences in flow separation patterns and pressure recovery are shown by the pressure distributions throughout the airfoil surfaces, which affects the airfoils' overall aerodynamic performance. By weighing trade-offs between lift, drag, and stability requirements, aerospace engineers and designers can choose the best airfoil for a given application. All things considered, this study advances our knowledge of airfoil aerodynamics and lays the groundwork for future investigations. To improve understanding and hone aerodynamic design processes, future research could examine more airfoil geometries, operating situations, and sophisticated computational tools. The efficiency, performance, and safety of aircraft systems can be further enhanced by deepening our understanding of airfoil behaviour.

Declaration of competing interest

The authors declare that they have no known competing financial interests or personalrelationships that could have appeared to influence the work reported in this paper.

Acknowledgement

This work was supported by UGC Research Grant (2021-2022), University of Dhaka, Bangladesh. This work was carried out using the computational facilities available in the Department of Applied Mathematics, University of Dhaka, Bangladesh.

References

1. Heppenheimer, T. A., 2003. The Wright Brothers and the Invention of the Aerial Age, Smithsonian National Air and Space Museum, Washington, DC.
2. Schmitz, F. W., 1976. Aerodynamics of the Airplane, NASA Translation, Washington, DC: NASA.
3. Liyana, M. et al., 2019. Flow Analysis of NACA 2412 Airfoil Using Pressure-Based Solver and k–ω SST Turbulence Model. Journal of Mechanical Engineering Research, **12(2)**, 45-52.
4. Lehmkuhl, O., A. Oliva, C. D. Pérez-Segarra and R. Borrell, 2010. Assessment of SGS Models for LES of Transitional Flows Using DNS Data, Computers & Fluids, **39(5)**, 853-864.
5. Baez, L., M. Rodríguez and P. Rodríguez, 2009. Laminar Separation Bubbles in Low-Reynolds-Number Airfoil Aerodynamics, AIAA Journal, **47(6)**, 1533-1542
6. Kunz, M. J. and I. Kroo, 1990. INS2D: A Two-Dimensional Incompressible Navier-Stokes Solver Using Artificial Compressibility. Technical Report, Department of Aeronautics and Astronautics, Stanford University.
7. Abbott, I. H. and A. E. von Doenhoff, 1959. Theory of Wing Sections, Including a Summary of Airfoil Data. Dover Publications, New York.
8. Hoarau, S., 2004. Lift and Drag Characteristics of NACA 0012 at Low Reynolds Numbers: DNS Studies. Physics of Fluids, **16(2)**, 350-362.
9. National Advisory Committee for Aeronautics (NACA), 1933. Technical Description of NACA 4412 Airfoil. NACA Report 460.
10. Selig, A. S. and M. D. McGranahan, 2004. Wind Tunnel Aerodynamic Tests of Six Airfoils for Use on Small Wind Turbines. NREL/SR-500-34515.N.
11. Douvi, N., K. Margaris and A. Margaris, 2010. Numerical Study of NACA 0012 Airfoil Using Turbulence Models at Various Angles of Attack. Journal of Mechanical Engineering Science, **224(9)**, 1999-2011.
12. Mittal, S. and T. Tezduyar, 1996. Finite Element Methods for Incompressible Flows at Low Reynolds Numbers. International Journal for Numerical Methods in Fluids, **22(7)**, 933-951.
13. Sogukpinar, H., 2018. The Effects of NACA 0012 Airfoil Modification on Aerodynamic Performance Improvement and Obtaining High Lift Coefficient and Post-Stall Airfoil. AIP Conference Proceedings. DOI: 10.1063/1.5025955.
14. Allmaras, S. R. and F. T. Johnson, 2012. Modifications and Clarifications for the Implementation of the Spalart-Allmaras Turbulence Model. Proceedings of the Seventh International Conference on Computational Fluid Dynamics (ICCFD7), 1902, 1-11.
15. Mihic, S., 2011. CFD Investigation of Metalworking Fluid Flow and Heat Transfer in Grinding. The University of Toledo.
16. Faber, T. E., 1995. Fluid Dynamics for Physicists. Cambridge University Press.
17. Elgeti, S. and H. Sauerland, 2016. Deforming Fluid Domains Within the Finite Element Method: Five Mesh-Based Tracking Methods in Comparison. Archives of Computational Methods in Engineering.
18. Sarrate Ramos, J., E. Ruiz-Gironés and F. J. Roca Navarro, 2014. Unstructured and Semi-Structured Hexahedral Mesh Generation Methods. Computational Technology Reviews.
19. Ali, Z., P. G. Tucker and S. Shahpar, 2017. Optimal Mesh Topology Generation for CFD. Computer Methods in Applied Mechanics and Engineering.
20. Eça, L., F. S. Pereira and G. Vaz, 2018. Viscous Flow Simulations at High Reynolds Numbers Without Wall Functions: Is y+ ≃ 1 Enough for the Near-Wall Cells? Computers & Fluids.
21. Julian, J., R. Difitro and P. Stefan, 2016. The Effect of Plasma Actuator Placement on Drag Coefficient Reduction of Ahmed Body as an Aerodynamic Model. International Journal of Technology, **7(2)**, 306-313.
22. Harinaldi, H., B. Budiarso and J. Julian, 2016. The Effect of Plasma Actuator on the Depreciation of the Aerodynamic Drag on Box Model. AIP Conference Proceedings, 1737(1).
23. Karpik, A., F. Cosco and D. Mundo, 2023. Higher-Order Hexahedral Finite Elements for Structural Dynamics: A Comparative Review. Machines, **11(3)**.
24. Matsson, J. E., 2023. An Introduction to ANSYS Fluent 2023, SDC Publications.
25. Gear, C., 1971. Simultaneous Numerical Solution of Differential-Algebraic Equations. IEEE Transactions on Circuit Theory, **18(1)**, 89-95.
26. Abbott, I. H. and A. E. Von Doenhoff, 1958. Theory of Wing Sections Including a Summary of Airfoil Data, Dover Publications, New York, 131-147.
27. Li, L. B., Y. W. Ma and L. Liu, 2012. Numerical Simulation on Aerodynamics Performance of Wind Turbine Aerofoil. Proceedings of the World Automation Congress (WAC), IEEE, 1-4.